Experiments in Fluids (2021) 62:193
https://doi.org/10.1007/s00348-021-03278-5

RESEARCH ARTICLE

Low-density multi-fan wind tunnel design and testing for the Ingenuity Mars Helicopter

Marcel Veismann[1] · Christopher Dougherty[1] · Jason Rabinovitch[2,3] · Amelia Quon[2] · Morteza Gharib[1]

Received: 30 April 2021 / Revised: 15 July 2021 / Accepted: 25 July 2021

Abstract

Prior to its successful flights on Mars, the Ingenuity Mars Helicopter system underwent extensive flight dynamics testing in the 25-ft Space Simulator facility, a low pressure environmental chamber at NASA's Jet Propulsion Laboratory (JPL), which can re-create relevant Martian conditions on Earth. This facility, while large, is not large enough for free or tethered forward flight tests. In this work, an open-jet, multi-fan wind tunnel concept is presented, which was integrated into the JPL facility to simulate the external freestream flow of forward flight scenarios in a low-density environment. A theoretical and experimental analysis was performed to evaluate the possibility of utilizing commercially available 80 x 80 mm axial flow cooling fan units for this type of wind tunnel. Sub-scale tests found that under Martian conditions, fans deliver approximately 30% reduced flow rates for the same RPM compared to Earth conditions due to decreased efficiencies at low Reynolds numbers. However, fans can run at higher RPM in low-density fluids, with the RPM increase being specific to the fan motor. While power consumption dropped by more than 90%, fans experienced higher thermal loads due to reduced heat convection. The study concludes that the investigated type of cooling fan can operate without modification in a low-density environment, offering a low-cost and easily adaptable wind tunnel solution. Informed by ambient flow field measurements on a comparable multi-fan wind tunnel, a low-density full-scale facility with 441 individually controlled fan units was constructed and used for aerodynamic testing of an engineering model of Ingenuity.

✉ Marcel Veismann
mveisman@caltech.edu

Christopher Dougherty
cdougher@caltech.edu

Jason Rabinovitch
jrabinov@stevens.edu

Amelia Quon
amelia.l.quon@jpl.nasa.gov

Morteza Gharib
mgharib@caltech.edu

[1] California Institute of Technology, 1200 E. California Blvd., Pasadena, CA 91125, USA

[2] Jet Propulsion Laboratory, California Institute of Technology, 4800 Oak Grove Dr., Pasadena, CA 91109, USA

[3] Present Address: Stevens Institute of Technology, 1 Castle Point on Hudson, Hoboken, NJ 07030, USA

Published online: 01 September 2021

Graphic abstract

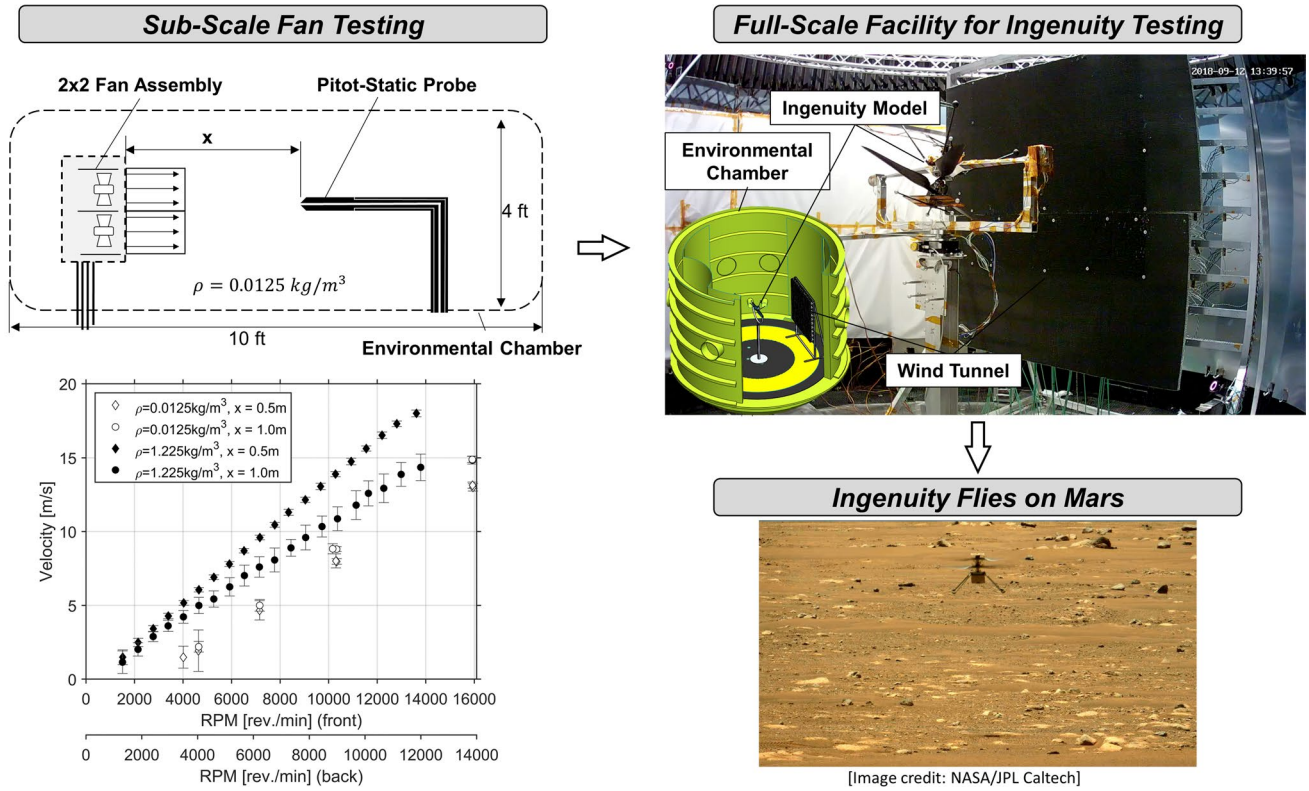

1 Introduction

The Mars 2020 rover mission, which launched on July 30, 2020, is searching for microbial life in rock and soil samples taken on the surface of Mars, and will prepare these samples for a possible return to Earth (NASA 2014). One particularly novel aspect of this mission is that the main Perseverance rover is accompanied by a small-scale rotorcraft named Ingenuity for a technology demonstration of rotorcraft flight under non-terrestrial conditions. Ingenuity's first successful flight on Mars took place on April 19, 2021, making it the first rotorcraft to fly on another planetary body.

Given the complete lack of in situ operational data for this class of unmanned aerial vehicles, Ingenuity's design had to undergo an extensive test campaign, to validate the feasibility of operation under Martian conditions. With the profound differences between Mars' and Earth's atmosphere (~1% of density as well as ~1/3 of gravity compared to Earth), these tests necessitated specialized facilities with suitable instrumentation that are capable of re-creating the relevant environmental conditions on Earth. In this context, JPL has been utilizing the 25-ft Space Simulator (Harrell and Largould 1969) with a gravity offload or reduced-weight prototypes to demonstrate the rotorcraft's hover capabilities under Mars representative conditions (Balaram et al. 2018). However, any translational movements were restricted within the space of the environmental chamber, which is why the investigation of forward flight scenarios required the use of a wind tunnel facility to simulate the external, nonzero freestream velocity. These tests were intended to investigate vehicle flight dynamics in forward flight (such as general stability characteristics), and to help inform optimal flight controller gain settings. Meanwhile, an exact full aerodynamic system identification was of secondary interest during this test, which helped relax the overall wind tunnel flow uniformity and size requirements.

Typically, wind tunnel investigations under non-standard atmospheric conditions are either performed in hermetically sealed facilities or in wind tunnels contained within environmental chambers. Currently operated Mars wind tunnels, specifically adapted for extremely low pressures and densities, are predominantly used for studying aeolian transport on Mars and are often driven by high-pressure air ejected through a series of orifices (White 1987; Wilson et al. 2008; Anyoji et al. 2009). A common finding for this type of wind tunnel is the relatively small test section size, which can be

explained by the extensive containment necessary for the extremely low atmospheric pressures. One such pressure-driven facility is the MARSWIT, an open circuit boundary layer wind tunnel contained within the Planetary Aeolian Laboratory (PAL), which could previously be utilized for the study of isolated rotor performance in forward flight at Martian atmospheric densities (Ament and Koning 2018). However, a full-scale engineering model of Ingenuity could not be tested in this facility due to an insufficient test section size.

This motivated the decision to design and integrate a dedicated wind tunnel facility into the 25-ft Space Simulator at JPL previously utilized for the Ingenuity hover tests. Driven by the mission's firm launch window and a limited access to the environmental chamber, commissioning of this system was subject to a rigid time frame (see Table 1), thus precluding custom air-movement equipment with specially adapted blade aerodynamics and prolonged procurement processes; commercially available off-the-shelf parts were required. Consequently, the design chosen was based on an open-jet, multi-fan wind tunnel concept utilizing 80 x 80 mm axial cooling fans, offering a simple and cost effective solution. Multi-fan wind tunnels, in general, are multi-source facilities with each fan individually addressable that allow the active generation of temporally as well as spatially evolving flow fields, such as forced turbulence (Ozono and Ikeda 2018), and have recently shown to be particularly suitable for replicating realistic wind and weather conditions for testing unmanned aerial systems (Noca et al. 2019). While the forward flight campaign of Ingenuity only required spatially uniform and steady flow fields, the multi-fan concepts further offered a number of benefits for the specific application: (1) modularity, allowing comprehensive sub-scale performance evaluations prior to commissioning a full-scale facility and providing the possibility to adjust the wind tunnel size and geometry at an advanced stage of the design process, (2) electrical connections for powering the system being more manageable than pneumatic lines for high-pressure driven systems, and (3) a large usable test section area compared with its effective footprint as well as reduced mixing lengths compared to single-fan facilities, making these wind tunnels a suitable candidate for use in space-limited environments that otherwise could not accommodate wind tunnel testing.

This study is aimed at evaluating the operational behavior and limitations of the selected off-the-shelf fan models under extremely low pressures and densities with a primary focus on the supplied flow velocities and the practicality of utilizing them for a Mars relevant wind tunnel system. This paper covers a predictive analysis of axial fan performance under varying-density conditions, an experimental sub-scale, low-density validation campaign, ambient spatial flow field measurements, and design aspects of the full-scale facility, which was ultimately used for aerodynamic testing of the Ingenuity engineering model.

Table 1 Project timeline overview and key milestones

Date	Milestone
7/2017	Official project start
8/2017	Theoretical first-order feasibility study
9/2017–1/2018	Sub-scale test campaign
2/2018–5/2018	Wind tunnel sizing experiments
2/2018–5/2018	Facility design
5/2018–6/2018	Facility construction & integration
7/2018	Dry run tests
8/2018–9/2018	Ingenuity tests in 25-ft Space Simulator
10/2018	End of 25-ft Space Simulator access and review of Ingenuity system for inclusion in the Mars 2020 mission

2 Martian environmental conditions

The composition of the Martian atmosphere primarily consists of CO_2 (95.3%), N_2 (2.7%) and Ar (1.6%) with trace amounts of O_2 and CO. Characteristic surface-properties of the Mars atmosphere are listed in Table 2 (Leovy 2001; Petrosyan et al. 2011), in comparison with Earth, defined by the International Standard Atmosphere. Note that these are representative values, which are subject to diurnal, seasonal, as well as global variations. Compared to Earth, density, pressure, and temperature as well as the gravitational acceleration at the Martian surface are substantially lower, and as a consequence, simulation of these conditions in a laboratory requires dedicated environmental test chambers. While the difference in gravity between Mars and Earth cannot be replicated in these low pressure facilities, dynamic scaling of models or gravity off-loads can be used to account for this difference. The most common approaches to replicate the atmospheric properties at the Martian surface inside an environmental chamber are: (1) a simplistic pump-down of standard air to approximate

Table 2 Characteristic Martian atmospheric properties (Leovy 2001; Petrosyan et al. 2011) compared to the Earth standard atmosphere definitions and approximate test conditions

Property	Units	Mars	Earth	Test (air)
Pressure, p	Pa	700	101325	1000
Density, ρ	kg/m^3	0.015	1.225	0.012
Temperature, T	K	220	288	297
Gravity, g	m/s^2	3.72	9.81	9.81
Kin. Viscosity, ν	$\times 10^{-5}$	100	1.46	156

Martian pressure and density, or (2) a full evacuation to vacuum and back-filling with CO_2 to representative pressures. All low-density experiments presented in this study were performed at a gas composition of that of Earth and at room temperature, utilizing the method of a simplistic pump down of air. The difference to the Mars composition is thought to be negligible for non-critical Mach number applications (Ament and Koning 2018). The resulting atmospheric properties for the adopted test conditions in this study are equally listed in Table 2. Density and viscosity of the test conditions were calculated assuming ideal gas law and Sutherland's law, respectively.

Given the extremely low fluid densities investigated, it is worthwhile to examine if continuum mechanics formulations are valid in this context. The standard criteria for evaluating if a flow is in the continuum regime is the dimensionless Knudsen number:

$$Kn = \frac{\lambda}{L}, \text{ with } Kn < 0.01 \text{ for continuum flows} \tag{1}$$

where λ is the mean free path of gas molecules in the fluid and L is a characteristic length scale. Representative values for λ for the Mars atmosphere have been reported to be on the order of 10 μm (Zhang et al. 2018; Bardera et al. 2020). Selecting the fan diameter ($D = 74$ mm) as the characteristic length yields a flow rarefaction of $Kn = 1.35 \times 10^{-4} \ll 0.01$, which is well below the critical threshold, and thus, this fluid system can be considered a continuum flow. A further consideration for this incompressible flow application is the Reynolds number,

$$Re = \frac{VL}{\nu} = \frac{\Omega D^2}{2\nu} \tag{2}$$

with V being a characteristic velocity, L a characteristic length, and ν the kinematic viscosity of the fluid. For fan applications, it is appropriate to select the tip speed, ΩR, as the characteristic velocity and the rotor diameter, D, as the characteristic length. Thus, for a geometrically similar solution, with similar operational parameters the difference in Reynolds number is:

$$\frac{Re_{earth}}{Re_{mars}} = \frac{\nu_{mars}}{\nu_{earth}} \approx 68 \tag{3}$$

This implies that viscous-related effects are more significant in fluid systems operating under Mars surface conditions compared to similar systems under Earth conditions.

3 Equipment/Facilities

Full-scale vehicle testing in a Mars equivalent density environment was desired at JPL for the Ingenuity test campaign in order to minimize the reliance on dynamic scaling of test conditions to Mars flight conditions.

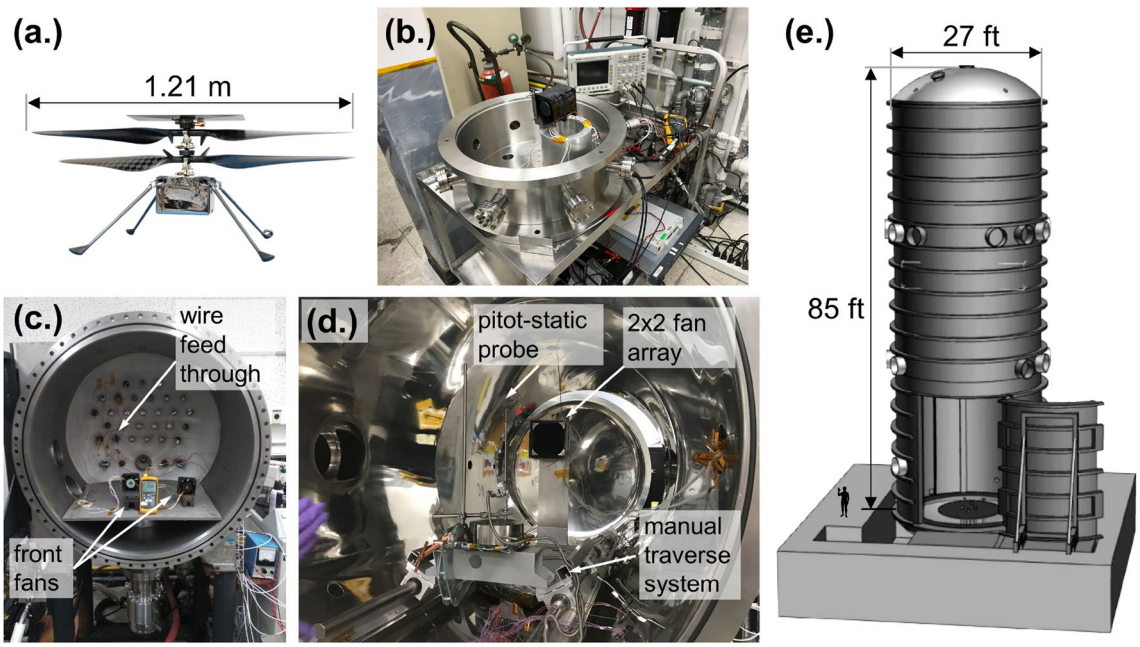

Fig. 1 Ingenuity Mars Helicopter system (NASA 2014) (**a**) and environmental chambers (diameter x height/depth): (**b**) 0.5 m × 0.7 m chamber, (**c**) 0.9 m × 0.8 m chamber, (**d**) 1.2 m × 3.0 m chamber, and (**e**) 8.2 m × 26.9 m JPL 25-ft Space Simulator (McCoy et al. 2016)

3.1 Ingenuity

The final design of the autonomous Ingenuity system (see Fig. 1a) has a gross mass of ~1.8 kg, featuring two counter-rotating two-bladed rotors with a diameter of 1.21 m in a coaxial arrangement to maximize thrust and efficiency for a size-limited vehicle footprint (Grip et al. 2018). In previous experimental campaigns, a full-scale prototype has been flown under simulated Mars atmosphere conditions in JPL's 25-ft Space Simulator (Balaram et al. 2018), validating both hover and axial flight capabilities. Furthermore, the performance of isolated single and dual rotors, similar to those of Ingenuity, was previously experimentally investigated under forward flight conditions in the Martian Surface Wind Tunnel (Ament and Koning 2018). This campaign, however, could not account for a rotorcraft fuselage and sufficient ground clearance due to limited facility size. Thus, a full-system forward flight investigation was most suitably conducted with integration of a dedicated wind tunnel facility into a sufficiently large environmental chamber to simulate the relative freestream expected during nominal forward flight operation of the vehicle. These freestream properties and test requirements for the wind tunnel were a uniform velocity field of up to 10 m/s over the complete helicopter with sufficient spatial margins and test durations of greater than 60 s. While the low inertia of these relatively small fans allows for quick ramp up times compared to single-fan-facilities, which enables simulation of gust conditions to some degree, the Ingenuity tests only investigated the system's response to steady uniform flow fields. This was due to a limited access to the 25-ft Space Simulator and was justified from an operations standpoint, since Ingenuity flights were scheduled to occur at times on Mars when wind speeds are expected to be minimal and within the allowable operating envelope.

3.2 Environmental chambers

The facility primarily utilized for full-scale testing of the Ingenuity Mars Helicopter aerodynamics and flight controls is the 25-ft Space Simulator (see Fig. 1e). This large cylindrical vessel, approximately 8 m in diameter and 27 m high, is capable of replicating high vacuum scenarios up to 10^{-6} Torr (Harrell and Largould 1969), making it a suitable test bed for a Mars Helicopter. While hover flight investigations have been performed in a free flight configuration (with a gravity offload tether or reduced-weight prototypes), the forward flight tests were intended to be performed with the craft fixed-mounted, upside down to a load cell, with approximately 3 m ground clearance. The inverted orientation was chosen to circumvent ground effect aerodynamics. Though the 25-ft Space Simulator is well suited for full-scale prototype testing, an expensive and lengthy pump-down process is required for a chamber of this size. As such, sub-scale fan validation tests were conducted in smaller environmental chambers whenever possible, shown in Fig. 1b–d. The use of the 25-ft Space Simulator is furthermore subject to extremely strict cleanliness and contamination requirements, with specific attention given to the tendency of lubricants and polymer materials to outgas in low pressure environments, with potential to deposit foreign particulates onto chamber walls and instrumentation. Consequently, a contamination evaluation needs to be performed on all equipment before integration into this facility, which is explained in greater detail in the sub-scale testing campaign. Based on standard protocol, the PVC-based (polyvinyl chloride) power and signal wiring was replaced on all fan units to meet contamination requirements. These component modifications were purely motivated by containment control precautions and are generally not a requisite for operation of the fan units in low-density environments.

3.3 Pitot-static systems

Three separate types of pitot-static systems were used for fluid velocity measurements, one for ambient and two for low-density conditions. For the latter, a *MKS Type 226AD Baratron* differential capacitance manometer with a 0.2 Torr (27 Pa) full-scale measurement range was used throughout the sub-scale test campaign. For flow velocity measurements of the full-scale facility, which were performed at a later stage of the project, a *MKS Type 120AD Baratron* high-accuracy differential pressure transducer with a 1 mmHg (133.3 Pa) full-scale range was employed alongside two *226A Baratron*. Despite featuring a wider measurement range, the *120AD* transducer has a superior accuracy and resolution (0.08% of Full Scale (F.S.) and 1×10^{-6} of F.S.) compared to the *226AD* transducer (0.3% F.S. and 0.01% F.S.). Previous studies of pitot-static measurements at low Reynolds numbers have shown that the inviscid assumptions of the Bernoulli equation are valid within 1% accuracy for $Re = \rho V_\infty R_{outer}/\mu > 45$ for hemispherical noses (Boetcher and Sparrow 2007). Below this threshold, the pressure coefficient c_p starts to deviate from the standard Bernoulli interpretation of $c_p = 1$, with $c_p > 1$ at low Reynolds numbers due to the effect of viscosity. For the dimensions of the here employed pitot-static tubes ($R_{outer} \approx 8$ mm), the critical freestream velocity at low densities, below which Reynolds number effects become significant, is $V_\infty \approx 10$ m/s. Consequently, all low-density velocity measurements were corrected for these viscous-related errors, which were on the order of ~ 1%.

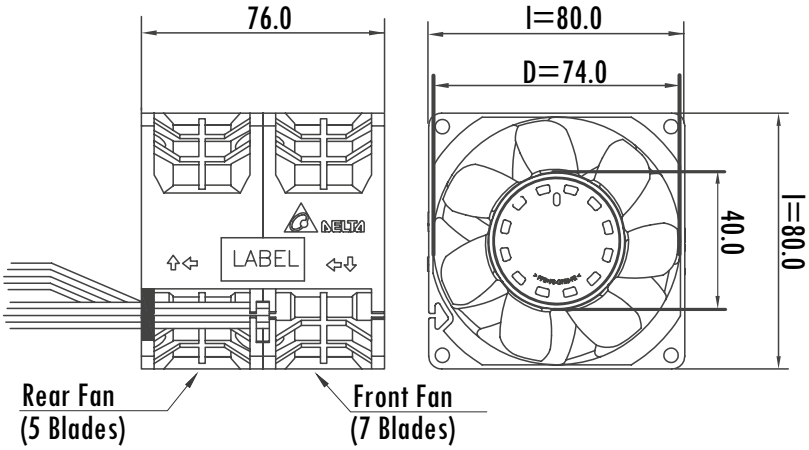

(a) Model: GFC0812DW-TD2G for sub-scale validation and ambient reference measurements (adapted from (Delta Electronics, Inc. 2016))

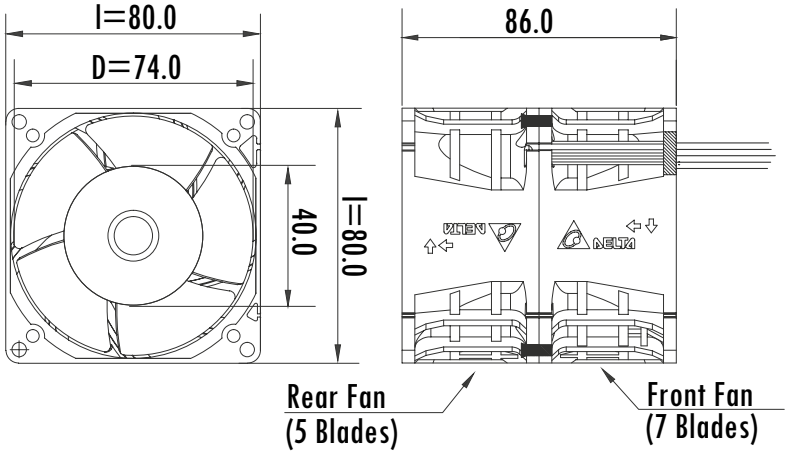

(b) Model: GFM0812DUB7S for the full-scale facility (adapted from (Delta Electronics, Inc. 2015))

Fig. 2 Technical drawings and terminology for fan units used in this work (measurements in mm). Note that the upstream fan is designated as the "Front Fan"

3.4 Axial fan units

The axial fans investigated throughout this study were commercially available DC fans (see Fig. 2), which are rated for a voltage of 12VDC and conventionally utilized in computer server air cooling applications. These square fan units ($l = 80$ mm) are comprised of two contra-rotating fan-rotors in series, operating at different rotation rates, and were selected as they provide one of the largest ratios of flow rate, Q_{max}, to total unit planform area, $A_u = l^2$, available for a fan this size. By using a contra-rotating system, the second impeller removes most of the swirl of the first impeller, recovering rotational energy and converting it to a static pressure rise. Therefore, these fans feature high airflows and static pressure and generate a much more directed flow compared to single-fan units. For the fans of this study, each of the two fan motors provides RPM-feedback of its respective rotor shaft via Hall effect sensors and can individually be controlled through user-commanded PWM inputs. The model from Fig. 2a was primarily utilized for the sub-scale validation and ambient reference tests, and is referred to in the following analysis unless otherwise specified. The fans specified maximum rotational speeds are: front fan (7 blades) 13,500 RPM/ back fan (5 blades) 11,000 RPM ±10%. No-load rotation rates of the brushless motors were determined by removing the fan rotors and were approximately 16,000 RPM and 13,000 RPM, respectively. At 100% duty cycle and $P_{max.} = 99$ W power consumption under standard conditions, this fan model delivers a maximum flow rate of $Q_{max.} = 5.0\,\mathrm{m}^3/\mathrm{min}$ at free delivery (i.e., zero static pressure), resulting in a theoretical wind tunnel freestream velocity of approximately 13.1 m/s ($V = Q/A_u$) when arranged in a large assembly. Due to supply shortages, the final full-scale facility was constructed with the fan model shown in Fig. 2b, which

features similar manufacturer specifications: front fan (7 blades) 13,800 RPM/ back fan (5 blades) 13,200 RPM ±10%, $P_{max.} = 108\,\mathrm{W}$, $Q_{max.} = 5.4\,\mathrm{m^3/min}$. For this replacement fan model, sub-scale and full-scale low-density velocity measurements were obtained and a life-cycle test campaign at Martian atmospheric conditions was performed.

4 Fan performance in low-density environments

A simplistic theoretical assessment of axial fan performance in low-density environments is presented in the following section, with particular attention given to the achievable flow speeds, power requirements and heat transfer. The following analysis considers single-rotor fan units for simplicity. More in-depth information on the estimation of maximum rotation rates and fan efficiencies as well as a close investigation of the heat transfer of fan units is provided in the supplementary material.

Lower densities have been shown to have considerable impact on fan performance. For general guidelines, the scaling laws for fan performance (Belady 1996) provide a first-order approximation of fan performance for geometrically and dynamically similar fans at various densities. These fan laws describe changes in volumetric flow rate, Q, total pressure drop, Δp, and fan power, P, as a function of the fan dimension, D, rotation rate n, and fluid density, ρ, as follows:

$$Q_2 = Q_1\left(\frac{D_2}{D_1}\right)^3\left(\frac{n_2}{n_1}\right) \tag{4a}$$

$$\Delta p_2 = \Delta p_1\left(\frac{D_2}{D_1}\right)^2\left(\frac{n_2}{n_1}\right)^2\left(\frac{\rho_2}{\rho_1}\right) \tag{4b}$$

$$P_2 = P_1\left(\frac{D_2}{D_1}\right)^5\left(\frac{n_2}{n_1}\right)^3\left(\frac{\rho_2}{\rho_1}\right) \tag{4c}$$

In this context, the subscripts '1' and '2' are used to refer to ambient reference conditions and low-density conditions, respectively. Note that according to the basic fan laws, the volumetric flow rate, and thus flow velocity, is considered independent of the density, and scales linearly with the fan rotation rate, while the pressure drop and power requirement decrease linearly with density for a given RPM. Based on these relations, non-dimensional coefficients for the flow rate, pressure drop and power can be established for a specific machine design (Wright 1999):

$$\Phi = \frac{Q}{D^3\Omega} \qquad \Psi = \frac{\Delta p}{\rho D^2\Omega^2} \qquad \lambda = \frac{P}{\rho D^5\Omega^3} \tag{5}$$

with $\Omega = 2\pi n/60$ the rotational speed in rad/sec. The fan laws are applicable as long as geometric similitude is maintained and efficiencies are equivalent at the different operating points, with efficiency being defined as:

$$\eta = \frac{Q\Delta p}{P_{mech}} = \frac{Q\Delta p}{\tau\Omega} \approx \frac{Q\Delta p}{P_{el}\eta_{el}} \tag{6}$$

However, for large differences in Reynolds number between operating points, as is the case when comparing operations on Earth to Mars, equal efficiencies cannot be assumed, since low Reynolds numbers are generally associated with increased losses and lower efficiencies due to thicker boundary layers and longer laminar portions along the blade, making the flow more prone to separation. Below a critical machine Reynolds number, approximately 2×10^6 for axial fan operation (AMCA 2016), these Reynolds number effects are particularly significant and since these fans generally operate below this threshold under ambient as well as low-density conditions, the dependence of fan performance on Reynolds number needs to be considered here. In this context, various Reynolds number corrections for axial and centrifugal fan efficiencies have been suggested in the literature, with perhaps the most common scaling method being (Rütschi 1958; Pelz and Stonjek 2014; Heß and Pelz 2010):

$$\text{Ackeret: } \frac{1-\eta_2}{1-\eta_1} = \frac{1}{2}\left[1 + \left(\frac{Re_1}{Re_2}\right)^{0.2}\right] \tag{7a}$$

$$\text{Pfleiderer: } \frac{1-\eta_2}{1-\eta_1} = \left(\frac{Re_1}{Re_2}\right)^{0.1} \tag{7b}$$

$$Re = \frac{\Omega D^2}{2\nu} \tag{8}$$

While more recent efforts have attempted to provide more reliable predictions for scale effects in incompressible turbomachinery units, using the universal formulas from Eq. 7 is convenient here, because technical specifications about the utilized fan models are limited. Along with the fan efficiency, flow and pressure coefficients have been observed to decrease with Reynolds number while the power coefficient usually increases. However, the scaling for these coefficients is less established compared to the efficiency scaling, particularly for axial fans. Corrections for the pressure coefficient have been proposed by presuming that pressure losses are equivalent to efficiency losses (Heß and Pelz 2010; Bogdanović-Jovanović et al. 2016; Pelz and Stonjek 2014; Wright 1999):

$$\frac{\Psi_2}{\Psi_1} = \frac{\eta_2}{\eta_1} \tag{9}$$

with no correction to the flow or power coefficient. Meanwhile, an alternative efficiency scaling has been suggested by Casey (Casey 1985) by considering the relative surface roughness along with the Reynolds number, with efficiency-dependent corrections for Φ and Ψ given as (Strub et al. 1987; Simon and Bülskämper 1984):

$$\frac{\Psi_2}{\Psi_1} = \frac{1}{2} + \frac{1}{2}\left(\frac{\eta_2}{\eta_1}\right) \tag{10a}$$

$$\frac{\Phi_2}{\Phi_1} = \left(\frac{\Psi_2}{\Psi_1}\right)^{\frac{1}{2}} \tag{10b}$$

and using $\lambda = \Phi\Psi/\eta$

$$\frac{\lambda_2}{\lambda_1} = \left(\frac{1}{2} + \frac{1}{2}\left(\frac{\eta_2}{\eta_1}\right)\right)^{3/2}\left(\frac{\eta_1}{\eta_2}\right) \tag{11}$$

It is important to mention that η_2/η_1 for these corrections is calculated based on Reynolds number as well as relative surface roughness, but Eqs. 10 have been adopted here without modification using the efficiency scaling from Eq. 7, since no information regarding surface roughness was available for the here utilized fans. Furthermore, it should be noted that Eqs. 10 have been primarily evaluated against centrifugal pumps in the past, but have also shown potential to be applicable for axial fans (Wright 1999). Lastly, all corrections presented above for efficiency, flow, and pressure coefficients are strictly speaking only valid within a certain Reynolds number ratio and close to the point of best efficiency. Thus, predictions are not expected to be exact, but should suffice here for first-order approximations of trends for the axial fan performance under test conditions mentioned in Table 2.

Figure 3 illustrates the trends of fan performance coefficients and efficiency as a function of Reynolds number relative to the reference conditions of ambient operation, with the Reynolds number based on the front fan. The reference Reynolds number Re_1 and low-density Reynolds number Re_2 are explicitly marked in the figure. The resulting maximum fan performance values for operation at Re_2 (test conditions) are also presented in Table 3. The value of Re_2 has been accounted for in increasing maximum fan rotation rates with reduced loading of the rotor in the low-density environment. Assuming that the torque of a fan is proportional to the fluid density and the square of the fan rotation rate as well as a linear speed-torque characteristic (i.e., linearly decreasing RPM with increasing motor torque demand) the maximum rotation rates of the front fan were estimated to be $n_2 = 15,957$ RPM, which is based on the motor rotation rate after removing the rotor ($n_0 = 16,000$ RPM). Furthermore, the reference efficiency was estimated to be $\eta_1 = 0.46$ at free delivery under ambient conditions. More information regarding these estimates is provided in the supplementary material. Figure 3 shows that with decreasing Reynolds number the ratios of Φ/Φ_1 and Ψ/Ψ_1 can be observed to decrease for a fan due to viscous-related effects, whereas the input power ratio, λ/λ_1, increases, leading to a power consumption that is larger than the linear decrease with density predicted by the basic fan laws. At the low-density operating point Re_2, the flow-coefficient-ratio-curve corresponds

Table 3 Comparison of ambient performance parameters for a dual fan-unit and expected values for low-density test conditions

Property	Units	Ambient	Test
Density, ρ	kg/m^3	1.225	0.012
Kin. Viscosity, ν	m^2/s	1.46×10^{-5}	1.56×10^{-3}
RPM (front/back)	1/min	13500/11000	15957/12980
Re (front)	–	2.65×10^5	2.94×10^3
$P_{el,max}$	W	99.24	5.14
Q_{max}	m^3/min	5.015	4.468

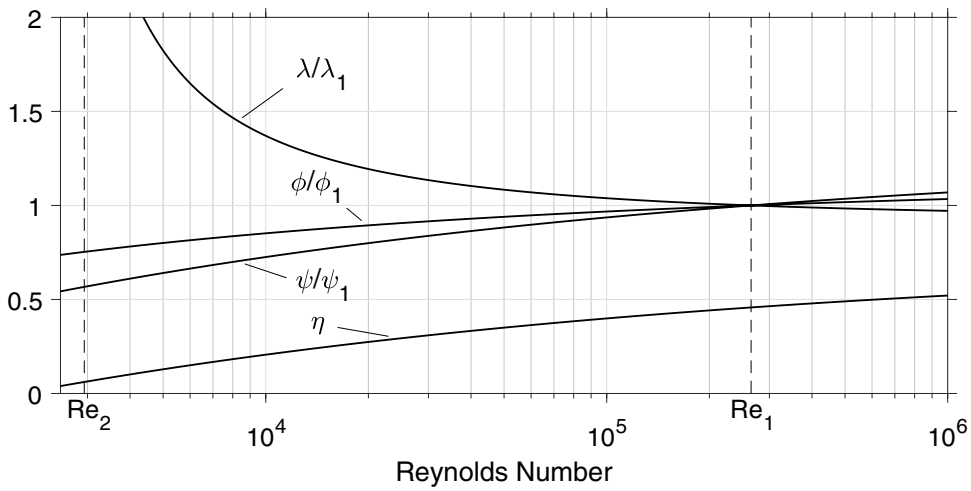

Fig. 3 Fan performance coefficients as a function of Reynolds number compared to ambient reference conditions at Re_1, using efficiency scaling of Ackeret

to approximately $\Phi_2/\Phi_1 = 0.75$, indicating that flow rate reductions of approximately 25% are expected for the same rotation rate. But accounting for an increase in rotation rate due to reduced aerodynamic loading, maximum flow rates on the order of 90% of those of ambient conditions are suggested for this fan model in Table 3.

Alongside the fan's flow rate and power consumption, the heat transfer is also severely affected by a changing fluid density, which critically influences the fan's capability to self-regulate internal heat. While the power consumption (and therefore the resistive joule heating) is significantly lower in low-density conditions, the lower density directly reduces mass flow as well as the heat transfer coefficient. Therefore, the fans are expected to experience slower initial temperature rise due to reduced power consumption compared to ambient conditions, whereas the reduced convective cooling and heat capacity will lead to higher steady-state component and exhaust temperatures. For a more comprehensive analysis of the fans' heat transfer properties in the low-density test conditions, readers are encouraged to consult the supplementary material.

5 Sub-scale testing campaign

To confirm the theoretical density scaling laws of fan operation previously presented, sub-scale tests were conducted in small environmental chambers shown in Fig. 1b–d. Since, as is shown in subsequent sections, the flow field initializes at the scale of each individual fan unit, the performance and flow evolution of one fan unit is representative of any greater array, provided the mixing behaviors of adjacent fans are accounted for. For uniform flow, the complex process of individual jet mixing can be ignored if the test apparatus is placed far enough downstream to allow individual fan flow fields to mix and merge on their own into a greater bulk flow. This enables a test campaign that, though considered sub-scale from an outer-array dimensional point-of-view, is dynamically similar from a flow-generation point-of-view when a chamber is evacuated to Mars-like densities, whether it be one, four, or 441 fan units employed for operation. The scope of this testing campaign, distributed over multiple tests, was: (1) evaluation of general functionality and contamination compliance, (2) flow velocity measurements on a 2x2 module assembly as a function of RPM and axial distance, and (3) life-cycle tests of a single unit.

5.1 Functionality (power, temperature, RPM) and contamination evaluation

An initial functionality test, involving two individual front fans from Fig. 2a (seven bladed rotor), was performed for evaluation of fan functionality in low pressure and density fluids with respect to controllability, rotation rates, and temperatures. To further investigate potential chamber contamination issues, two front fans were used in this test, one with the original ball bearing and lubrication and one with a metallic bushing, which was deemed more chamber-safe from contamination control. The PVC-insulated power and signal wires were presumed to not be contamination compliant and were replaced by chamber-safe, PTFE-jacketed (polytetrafluoroethylene) wires on both models and fans were "baked out" at 50 °C for 48 h to mitigate chamber contamination. For testing, the fans were placed inside an environmental chamber (see Fig. 1c) with the wiring fed through the chamber wall and the chamber was pumped down to 7 Torr (933 Pa) at a constant temperature of 22 °C. The functionality test consisted of periodic measurements of power, temperature, and rotation rates at continuous operation at 100% duty cycle over a time of 10 min. Since these types of fans are typically not equipped with temperature sensors, the fans were disassembled prior to testing and separate thermalin couples were installed in the fan are housing near the motor coils for internal temperature monitoring. Meanwhile, rotation rates were measured by the fans' built-in Hall effect sensors. The results in comparison with ambient reference measurements are illustrated in Fig. 4. The test confirmed a substantial decrease in power consumption by 94% and an RPM increase of 7.8%. As anticipated, the temperature history in the low-density environment displayed slower initial heating of

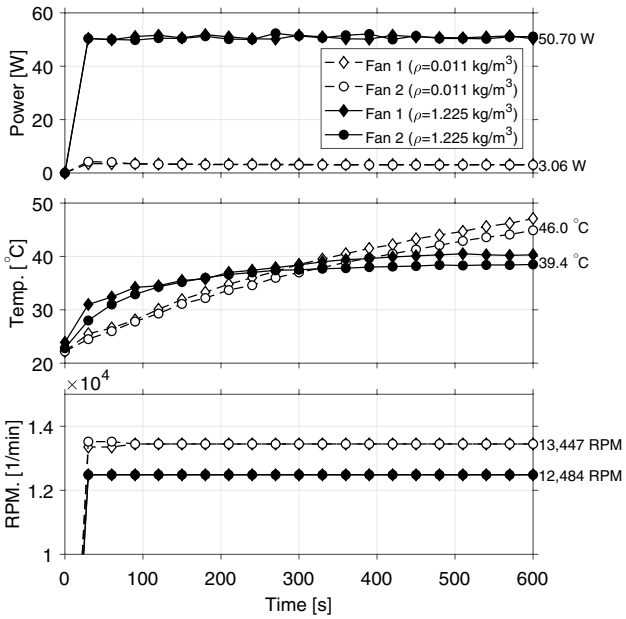

Fig. 4 Periodic performance measurements of two front fans (fan 1: bushing, fan 2: original ball bearing) operating under ambient and low-density conditions and terminal measurements at $t = 600$ s, averaged across both fans for each operating environment

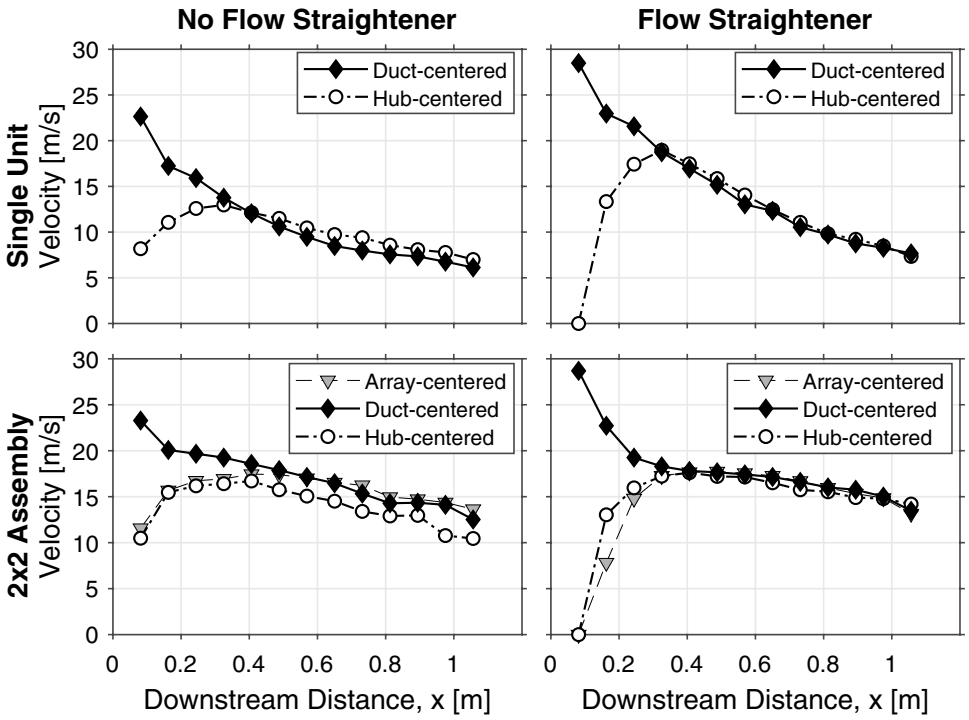

Fig. 5 Ambient velocity measurements of a single fan unit and 2x2 assembly with and without flow straightener (6.35 mm cell size, 508 mm depth)

the components compared to ambient conditions. However, while fan temperatures in the ambient tests start to level off at T = 39 °C after $t = 300$ s, the temperatures in low-density air continue to rise, even after $t = 600$ s with a maximum recorded temperature of T = 46.0 °C. This behavior is a logical conclusion to the reduced joule heating due to lower power consumption and the reduced convective cooling by the fluid, leading to longer settling times toward higher steady-state temperatures. Note that the recorded rotation rates during the tests were lower than the manufacturer specification under ambient conditions (13,500 RPM) and also lower than the predicted rotation rates for low-density (15,957 RPM).

It could be shown that these discrepancies can be traced back to the voltage drop associated with the additional cabling required to feed power and signal through the chamber wall and was accounted for in subsequent experiments by increasing power wire thickness (wire gauge). As can be seen in the following test (see Fig. 6), rotation rates in low-density environments are close to the predicted values when power wires are sized appropriately. Considering the above presented results and an internally specified acceptable thermal limit of 50 °C (more information on thermal loads is presented in the life-cycle test), continuous fan operation appears to be attainable for more than 600 s without overheating of components.

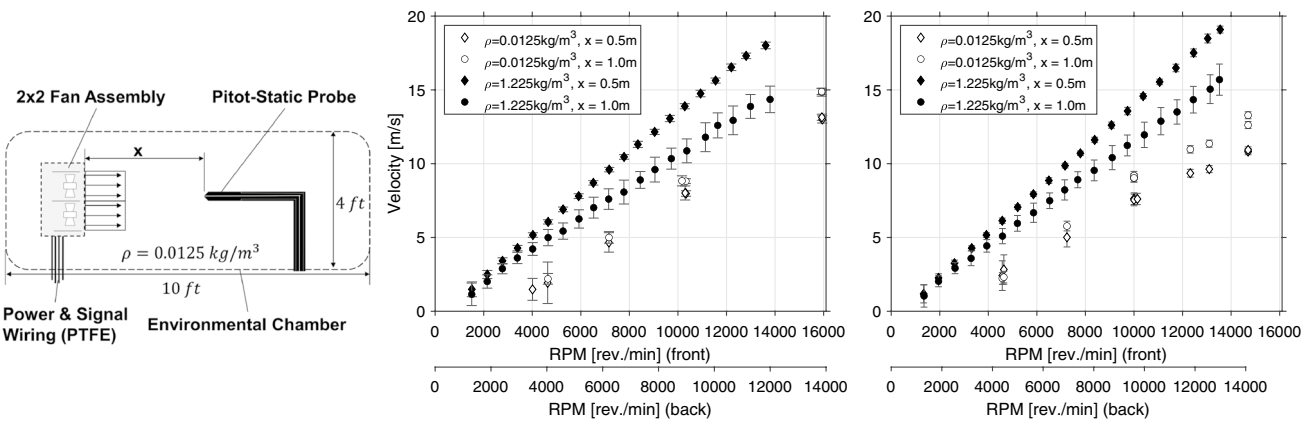

Fig. 6 Schematic setup (not to scale) and velocity measurements as a function of fan rotation rate and axial measurement distance for ambient and low-density conditions (left: model Fig. 2a, right: model Fig. 2b)

The performance of the two different fan units with different bearings was shown to be largely comparable. Furthermore, contamination measurements confirmed no outgassing behavior of the original ball bearing lubrication or any other polymer components of the fan unit. Therefore, no additional modifications to the fan units were required for operation within the environmental chambers aside from the wiring replacement. It has to be stressed that the wire replacement was only necessary due to the extreme cleanliness requirements specific to the 25-ft Space Simulator and is not essential for general operation of the fans in low-density fluids.

5.2 Velocity measurements

Pitot-static tests were performed to investigate the achievable flow velocities of these commercially available axial fan units in low-density environments. Prior to measurements in the environmental chamber, reference measurements under ambient conditions were performed to outline the most appropriate fan configurations and measurement location. These ambient baselines consisted of local mean flow velocities of a single fan unit as well as of a 2x2 fan unit assembly as a function of measurement location (axial and spanwise), and are shown in Fig. 5. Spanwise measurement locations were assigned downstream of the rotor hub, the fan duct, and the center of the fan array for the 2x2 assembly. The results show that the measurement location, number of fans, and flow manipulation have a profound impact on the measured local flow velocity. At axial distances below 0.4 m from the fan exit plane, the spanwise measurement location appears to be most significant, with high flow velocities downstream of the duct and low velocities at the hub and array center. Beyond this initial mixing distance ($x > 0.4$ m), the flow velocity measurements only minimally depend on the spanwise measurement location, while showing a consistent mean velocity decrease with increasing axial downstream distance for all configurations. As can be seen, increasing the number of fans yields more constant flow velocities with axial distance. This is to be expected as centerline velocity decay of a fluid jet scales with its diameter. Thus, as the overall diameter of the total fluid jet emerging from the fan face increases, the velocity decay is less significant along the center line for a given downstream distance. Figure 5, furthermore, indicates that adding a flow straightener to remove the swirling motion of the air flow aids in decreasing the velocity dependence on the axial and spanwise measurement locations. In this case, a flow straightener with circular cross-section shape was mounted flush to the fan face for ease of construction. Note here that the measured flow velocities were larger than the theoretically predicted value of $Q/A_u = 13.1$m/s under Sect. 3.4, which is believed to be due to a contraction and acceleration of the open-jet flow.

Under consideration of these ambient baselines, a 2x2 fan unit assembly with flush mounted flow straightener was selected as the most suitable configuration for the low-density tests with array-centered measurement locations and at downstream distances of $x =$ 0.5 m and 1.0 m. These low-density measurements were performed for both fans displayed in Fig. 2. The fan assemblies were separately installed inside an environmental chamber (see Fig. 1d), and representative flow velocity measurements in low-density air were obtained using a pitot-static system with an *MKS 120A Baratron* pressure transducer. A slightly larger chamber (4 ft. by 10 ft.) than was used for the initial functionality test was chosen to reduce the significance of wall effects, with the pitot-tube placed close to the center of the chamber. Figure 6 illustrates the measured averaged fluid velocities for low-density compared to ambient conditions as a function of the fan rotational rate and axial measurement distance. Low-density velocity measurements were corrected for low-Re, non-Bernoulli effects based on (Boetcher and Sparrow 2007). The experimental results confirm a near-linear increase in flow rate (and thus fluid velocities) with fan rotation rate as stated by the basic fan laws in Eq. 4. As anticipated, flow velocities for a given rotation rate are considerably lower for Martian fluid densities, on average 30% and 36% for the two investigated fan models, respectively, which is most likely due to the lower Reynolds numbers and therefore lower hydraulic efficiencies. These relative losses are even greater than predicted in Sect. 4, indicating that the universal scaling formulas may not be particularly accurate for these extremely low machine Reynolds numbers. As previously shown, the reduced motor loading also permits higher maximum rotation rates at 100% duty cycle, partly offsetting the effect of reduced flow rates. This relative maximum RPM-increase was found to differ between the fan models and was 17% and 8.5%, respectively, resulting in maximum flow speeds of $V_{2,max}/V_{1,max} = 0.863$ (left) and $V_{2,max}/V_{1,max} = 0.685$ (right) when averaged across both axial distances. The specific RPM increase is most likely due to different motor characteristics, which has been shown here to be a key factor determining the maximum flow speeds. The maximum RPM under simulated Martian densities can be easily determined experimentally under ambient conditions by simply removing the fan rotor from the motor shaft. Interestingly, while pitot-static measurements under ambient conditions show peak velocities at $x = 0.5$ m, maximum velocities in the low densities are consistently found at $x = 1.0$ m. It is unclear whether this is a facility-related effect or due to the reduced Reynolds number of the jet-like flow, resulting in different mixing and expansion properties.

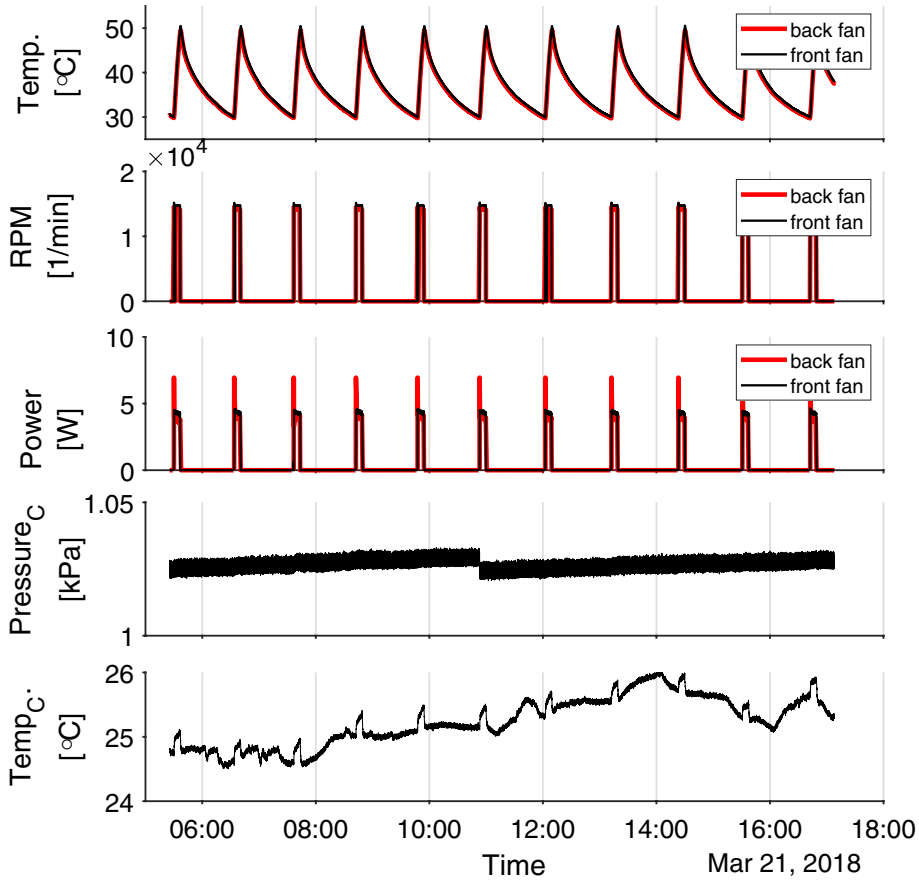

Fig. 7 Extract of sampled fan quantities during the life-cycle test. The subscript *C* is used to refer to the pressure and temperature of the chamber

5.3 Life-cycle test

A life-cycle test of a single fan unit (Fig. 2b) was performed in a bench-top vacuum chamber (see Fig. 1b) in air at pressures of 1025 Pa ($\rho = 0.011$ kg/m^3) and temperatures of 25 °C, evaluating product reliability and durability under non-design conditions. As specified by the manufacturers, the fans have a life expectance (L10) of 70,000 h of continuous operation at 40 °C (Delta Electronics, Inc. 2015. An extract of the sampled quantities throughout the test is illustrated in Fig. 7. In this life-cycle test, an off-the-shelf fan unit (front and back fan) with replaced fan wiring underwent repetitive operation at 100% duty cycle, starting at an internal component temperature of 30 °C, ending at 50 ∘C. The final temperature was reached within an average of 6.5 min, after which a more lengthy cool-down process occurred. While these fans are rated for operation at maximum temperatures of up to 70 °C (Delta Electronics, Inc. 2015), a more conservative upper temperature limit was chosen here since higher temperatures generally reduce the life expectancy of fans, approximately by a factor of 1.5 every 10 °C (Jin et al. 2012), and fan replacements in the environmental chamber were not feasible. The 50 °C limit allowed for acceptable operational times of the wind tunnel similar to those expected for the Ingenuity tests.

Over a total life-cycle test duration of approximately 710 h (30 d), 633 cycles were performed with a total time of operation of approximately 70 h. By the end of the life-cycle test, the components showed no signs of performance depreciation, excessive wear or malfunctioning due to potential lubrication outgassing, meeting the reliability requirements for a full-scale facility. During operation in the low-density environment, the total power draw of the front and back fans combined at 100% duty cycle was approximately 8.5 W, a reduction of approximately 92% compared the 108 W power consumption under ambient conditions. The recorded rotation rates were 14,750 RPM (front) and 14,050 RPM (back), which is consistent with the ones shown in Fig. 6 (right).

6 Open-jet flow field analysis

Flow field analysis under Earth-ambient conditions was performed on an existing open-jet multi-fan wind tunnel to establish the functional test section with uniform flow and low levels of turbulence. The facility used for this study was the multi-fan wind tunnel at the Center for Autonomous Systems and Technologies (CAST) at Caltech. This system is composed of 36x36 fans specified in Fig. 2a with a total fan area of $L^2 = 2.88$ m x 2.88 m, and has a flush mounted

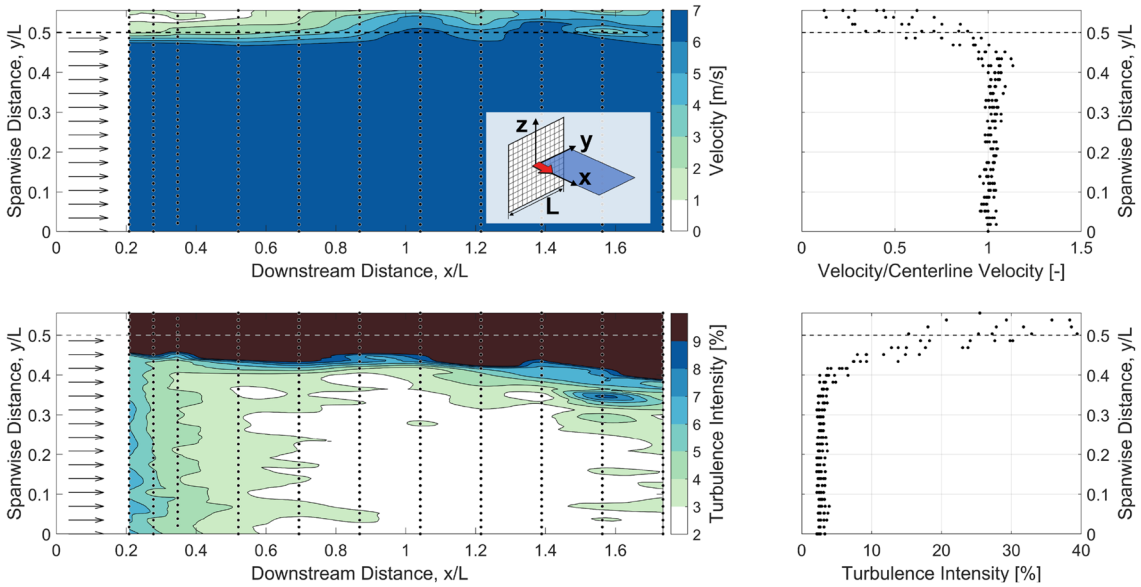

Fig. 8 Two-dimensional velocity and turbulence intensity field of a 36x36 open-jet multi-fan wind tunnel ($D = 74$ mm, $l = 80$ mm, $L = 2.88$ m) at 45% duty cycle with discrete measurement locations indicated as points (left), and collapsed spanwise measurements for $20D < x < 1.4L$ (right)

flow straightener for removing flow swirl. The maximum far field velocity, measured at 100% duty cycle, is approximately 14.3 m/s, which is generally lower than the maximum velocities measured for the equivalent 2x2 assembly at 100% duty cycle, but close to flow speeds at downstream distances of $x = 1.0$ m under ambient conditions (see Fig. 6). The lower values are assumed to be due to a stronger flow contraction and acceleration for smaller assemblies. Thus, the maximum far field velocity for large multi-fan assemblies was subsequently assumed to be equal to the velocities of a 2x2 assembly at $x = 1.0$ m.

Figure 8 shows the mean velocity and turbulence intensity fields of the wind tunnel operating uniformly at 45% duty cycle, measured using a hot-wire anemometer at various downstream and spanwise distances within the center plane of the wind tunnel. The spanwise and downstream distances were normalized by the overall wind tunnel dimensions, L, to facilitate comparison to other wind tunnel facilities. The mean velocity measurements indicate relatively consistent flow speeds within the core flow. At spanwise distances from the centerline of $y > 0.45L$ edge effects start to become significant, indicated by rapidly decreasing flow velocities. This is particularly evident when observing the collapsed measurements (right). Meanwhile, turbulence intensity can be observed to decay with downstream distance, x, and a region of comparable low turbulence intensity within the core flow can be identified. In this case, shear layer effects can be observed for $y > 0.4L$, where turbulence intensity values increase significantly with spanwise distance, rendering this part of the flow unsuitable for aerodynamic testing. Furthermore, the shear layer growth significantly narrows the functional test section with low turbulence levels beyond downstream distances of $x > 1.4L$. When establishing the lower downstream limit of the functional test section, it is worth noting that, given a sufficiently large number of fan elements, the downstream turbulence intensity evolution in the core flow does not change with the number of fans, but is more affected by the diameter of utilized fans (i.e., a further increase wind tunnel size does not affect downstream turbulence intensity levels within the core flow, while choosing smaller fans does). Therefore, the lower downstream limit of the functional test section is more appropriately characterized by the individual fan rotor dimension, D. In this case, the turbulence intensity decays with downstream distance, plateauing at values of $TI \approx 2.5\%$ at $x = 0.5\,L = 1.44$ m, corresponding to $x \approx 20D$ for the here employed fan model with $D = 74$ mm. For space constrained applications, where flow uniformity is of secondary concern, a minimum downstream distance of $x > 0.5$ m ($x > 6.75D$) should be maintained. This was previously indicated by the measurements in Fig. 5, where the individual jets from each fan mix within downstream distances of approximately 0.4 m – 0.5 m to a bulk flow. It has to be noted here that the lack of dedicated flow manipulation (e.g., meshes, grids) results in relatively high levels of turbulence intensity compared to conventional wind tunnel facilities utilized for precise aerodynamic identification. While the turbulence intensity was not a primary concern for testing of Ingenuity, further flow manipulation by means of perforated plates and screens as well as introducing a spacing between flow straightener and fans are viable

options to further improve flow uniformity, which, however, requires more extensive installations and reduces maximum flow velocities. Hence, for the most simplistic installation of a flush mounted flow straightener, a suitable test section can be determined to be ideally $y, z = [-0.4L, 0.4L]$ and $20D < x < 1.4L$, or $6.75D < x < 1.4L$ for space constrained installations.

Although these flow field results are for ambient conditions and may not necessarily be identical under low-density scenarios, they allow a rough estimate of the required wind tunnel size for the Ingenuity forward flight tests. Moreover, rotorcraft operation in the wind tunnel flow imposes further constraints on the test section size, which needs to be accounted for. In this context, rotorcraft experiments, similar to the Ingenuity forward flight tests with varying test section size, were performed on the CAST wind tunnel to outline, at which size edge effects become pronounced in the rotor forces. These results have been omitted here in the interest of space, but are available as supplementary material.

7 Full-scale facility overview and performance

This section briefly showcases key features of the full-scale facility (see Fig. 9), constructed for the Ingenuity forward flight test campaign, and is not meant to be comprehensive regarding design details. The facility is composed of a total of 441 dual-fan units specified in Fig. 2b. Power and signal wires of each fan were replaced with PTFE jacketed wires for chamber-contamination-related precautionary measures, which is, however, not a requisite for general functionality of the fan models in a low-density environment. Individual fan units were arranged into 3x3 modules, with each module holding its own control and power distribution board. The boards supported assigning individual PWM signals to each fan while monitoring all Hall-effect sensor information from each fan separately and were linked via a local network connection to a central computer. The total number of fans that could be sourced in time for the anticipated test schedule was limited to approximately 441 fan units, limiting the number of modules for the wind tunnel in the 25-ft Space Simulator to 49. The modules were mounted to an external frame in a square, 7x7 configuration, adding up to an array size of 1.68 m × 1.68 m. This arrangement was chosen, such that the Ingenuity rotors, with a diameter of $D = 1.21$ m, were appropriately placed within the core flow ($[-0.4L, 0.4L]$, see previous section) with sufficient margins in the spanwise direction to minimize edge effects. A flow straightener for flow swirl removal was added downstream of the fans and was mounted flush to the front face of the fans for ease of construction. DC power supplies were placed outside the environmental chamber, with main power wires fed through the chamber wall. At maximum performance the electrical power draw is approximately 3.7 kW. Due to the electrical supply limitations, the wind tunnel is only capable of operating in low-density environments, where the fan power consumption is considerably reduced. A custom, Python-based script provided an interface for the wind tunnel control, allowing the user to assign individual PWM to each fan separately while monitoring all RPM information simultaneously. While receiving RPM-feedback from each fan provided the possibility for a closed-loop facility control, only open-loop control (i.e., assigning identical PWM-values to each fan) was used to reduce code complexity and avoid oscillatory fan behavior associated with the closed-loop control. Nonetheless, the RPM information was utilized for wind tunnel status monitoring and fan failure detection. As a secondary feature to verify proper operation of the wind tunnel within the closed environmental chamber, an infrared

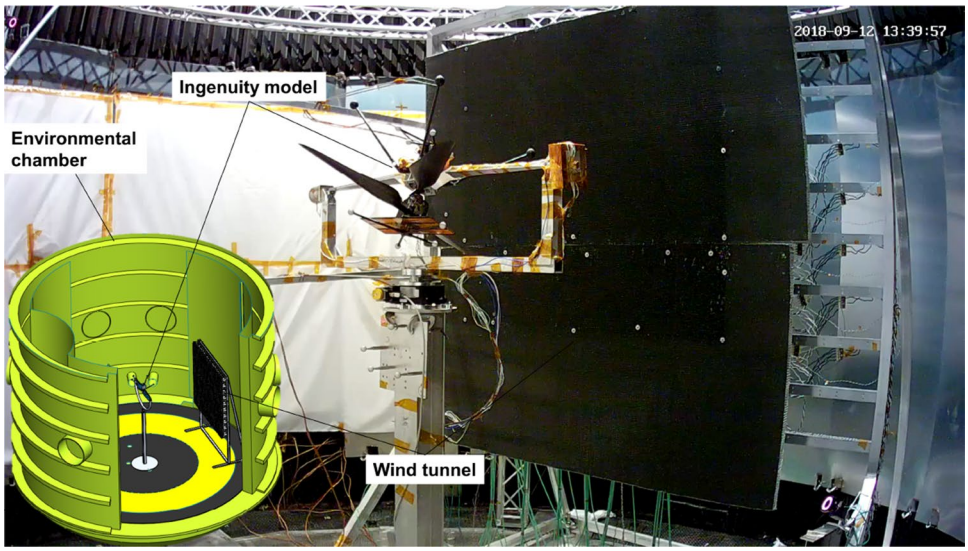

Fig. 9 Full-scale multi-fan wind tunnel facility inside the 25-ft Space Simulator for aerodynamic testing of the Ingenuity system

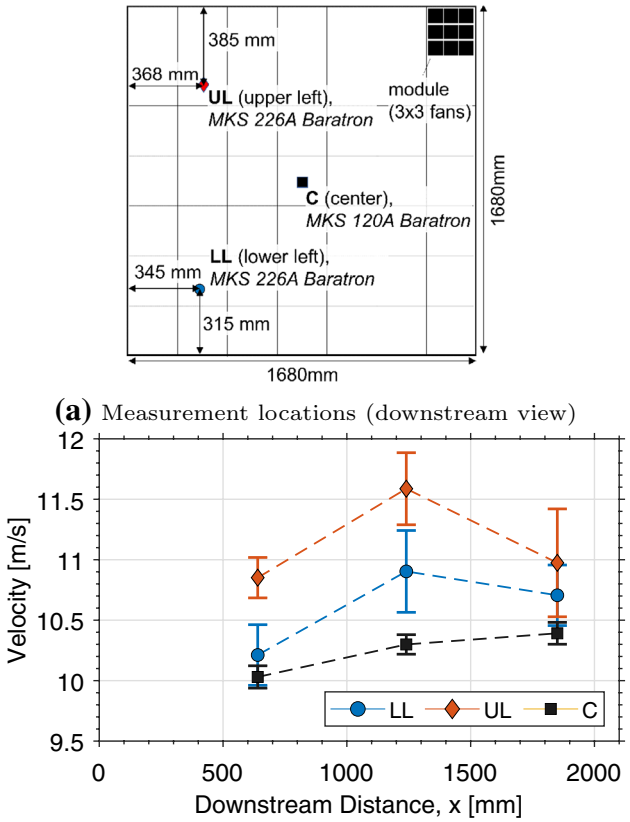

Fig. 10 Pitot-static measurements of the full-scale facility in low-density air ($\rho = 0.019$ kg/m^3). Error bars denote 2σ of the velocity time series

camera inside the chamber monitored fan temperature and, thus, functionality. In case of a physical failure or a wire disconnect, defaulting the fan to a high- or off-state, would reveal the specific fan unit as a thermal hotspot or darkspot, respectively, which allowed for defect or malfunctioning units to be identified quickly and reliably. It should be mentioned that throughout the entire Ingenuity test campaign, which involved a wind tunnel running time on the order of tens of hours, no mechanical fan failure occurred.

In order to verify fluid moving capabilities of the wind tunnel and to calibrate freestream velocities for assigned PWM values, multiple dry-runs under low-density conditions ($\rho = 0.019$ kg/m^3 and at room temperature) were performed prior to installing the Ingenuity engineering model. Figure 10 shows pitot-static mean velocity measurements for one dry-run at 100% duty cycle (averaged over 120 s) at various measurement locations relative to the tunnel and downstream distances using separate pitot-static probes which were mounted to a support frame. Downstream distances had to be manually adjusted, requiring a complete chamber evacuation and refill cycle for each distance. Viscous-related errors of the Bernoulli equation due to low Reynolds numbers were corrected for.

The velocity measurements in Fig. 10 at the center location are shown to be increasing with downstream distance to 10.4 m/s at 1.85 m. These values are marginally lower than those reported for a 2x2 assembly of the same fan model under comparable low-density conditions shown in Fig. 6 (right). This is consistent with previous findings under ambient conditions, in which flow velocities for a large multi-fan assembly were observed to be lower than for a 2x2 assembly and close to the velocities measured at downstream distances of $x = 1.0$ m. Since no ambient baselines for the full-scale facility (regarding fan choice and size) could be obtained, due to power limitations, the ambient maximum full-scale velocity was estimated to be 15.5 m/s based on the ambient 2x2 assembly measurements from Fig. 6 (right) at $x = 1.0$ m. This suggests that the far field, centerline velocities for this facility are approximately 30% lower for Martian atmospheric densities compared to Earth conditions. Even though the internal temperature of the fans increased over time while operating, no appreciable changes in the freestream velocity for a given PWM were observed.

The mean flow velocities as well as the error bars, here denoting the estimated measurement uncertainty of 2σ, can be found to be consistently larger for the corner locations compared to the center. It is unclear whether the differences are equipment related, or if they are physically manifested in the flow. It appears that shear layer effects start to manifest themselves in the measurements of the corner locations at distances of $x > 1.24$ m by increasing measurement uncertainty and decreasing mean velocities. This is particularly evident for the upper left measurement configuration. However, given the sparse amount of measurement points, this cannot be concluded with certainty and is left for more sophisticated analyses of the flow field within the environmental chamber in future studies. Nonetheless, these results provide further evidence that the presented multi-fan wind tunnel concept is functional under low-density conditions, delivering flow speeds that were estimated to be 30% lower than under ambient scenarios. It could also be shown that flow speeds at the corner locations are comparable with velocities at the center up to downstream distances of $x = 1.85$ m, designating this part of the test section as potentially usable for applications where the desired quantities of interest allow for the flow uniformity to vary by $\sim \pm 10\%$.

8 Conclusions

The material presented in this paper describes the performance evaluation of small, commercially available DC fan units under Martian atmospheric pressures and densities. These fans were ultimately arranged to form a much larger wind tunnel facility inside an environmental chamber for aerodynamic testing of the Ingenuity Mars Helicopter under relevant conditions.

In accordance with published literature, sub-scale tests under simulated Martian atmosphere verified decreasing fan efficiencies at the low machine Reynolds numbers, which manifest themselves in lower flow coefficients of approximately $30-36\%$, i.e., reduced flow rates for a given rotational speed. However, given the reduced rotor loading in the thin atmosphere, the fans' brushless motors showed increased maximum rotation rates between 8.5% and 17%, partly compensating for the decreasing flow rates. Therefore, maximum flow speeds of these off-the-shelf units are strongly dependent on the motor characteristics and the RPM-increase with decreasing fluid density. Meanwhile, the maximum power draw of the fan units dropped by around 90%. Due to reduced convective heat transfer in low-density fluids, components experience higher thermal loads, limiting test durations to 10 min during this study. By means of ambient flow field measurements on an analogous multi-fan wind tunnel, the required spatial margins could be determined. It is worth mentioning that the project's restrictive timeline and limited access to environmental chambers often made it prohibitive to complete a more in-depth analysis of the fan aerodynamics in these low Reynolds number fluids. Furthermore, the requirements for an open-jet configuration imposed by the Ingenuity forward flight tests made it difficult to precisely quantify the low-density effects on flow velocities due to the near field acceleration of the flow and a far field decrease in velocities, which varied depending on the fluid density as well as the wind tunnel size. Therefore, more research is needed to fully establish fan performance parameters in a fluid with properties that substantially deviate from ambient conditions. Nonetheless, functionality of multi-fan wind tunnels even under extremely low pressures was demonstrated, proving that flow speeds of up to 10 m/s are achievable. This study can help to open up new possibilities for low-speed aerodynamic testing with this unique class of wind tunnel systems, which are extremely versatile due to their modular design and are aptly suited for rapid integration into extreme environments. A successful test campaign for Ingenuity was completed with this newly developed low-density, low-speed, open-jet, multi-fan wind tunnel at JPL, and Ingenuity has now successfully demonstrated powered and controlled flight on Mars, making it the first rotorcraft to fly on another planetary body.

Supplementary Material

Estimation of fan efficiencies and maximum rotation rates in low-density environments

To predict the fan performance with varying Reynolds numbers based on Eqs. 7 and 10 requires an initial estimate of the efficiency at the reference Reynolds number, η_1 as well as information regarding the Re number at the test conditions. Lacking official information by the manufacturer, the efficiency at maximum flow rate and free delivery (zero static pressure) under ambient conditions was approximated via Eq. 6 and assuming that the total pressure rise equals the dynamic pressure of the flow within the fan duct:

$$\Delta p_1 = \frac{1}{2}\rho_1 {V_{d,1}}^2, \quad \text{with } V_{d,1} = Q_1/A_d \tag{12}$$

where A_d is the annular area of the fan duct. Using the manufacturer specified flow rate and power consumption at zero static pressure with an assumed electrical efficiency of $\eta_{el} = 0.85$ yields a fan efficiency of $\eta_1 \approx 0.46$.

For determining the machine Reynolds number at low-density test conditions, it also had to be considered that brushless motors of a fan can usually run slightly faster as density decreases due to reduced aerodynamic loading and a reduced torque demand. The steady-state torque of a fan can be assumed to be proportional the fluid density and to the square of the fan rotation speed $\tau = \tau(\rho, n^2)$, and was modeled here with the constant torque coefficient for a given geometry, which can be solved for the torque at low-density conditions:

$$\tau = C_Q \rho n^2 D^3 \tag{13}$$

$$\tau_2 = \tau_1 \frac{\rho_2 n_2^2}{\rho_1 n_1^2} \tag{14}$$

For a constant voltage applied to the motor terminals, it can be assumed that the brushless motor driving the fan has a simple linear speed-torque characteristic (i.e., linearly decreasing RPM with increasing motor torque demand):

$$n_2 = n_0 - \frac{dn}{d\tau}\tau_2 = n_0 - \frac{n_0 - n_1}{0 - \tau_1}\tau_2 \tag{15}$$

where n_0 is the motor speed under no-load conditions. Substituting Eq. 14 into Eq. 15 yields:

$$n_2 = n_0 - \left(\frac{\rho_2}{\rho_1}\right)\left(\frac{n_2}{n_1}\right)^2 (n_0 - n_1) \tag{16}$$

Using the front fan values of $n_0 = 16,000$ RPM and $n_1 = 13,500$ RPM for ambient conditions at $\rho_1 = 1.225$ kg/m^3 (see Sect. 3.4), Eq. 16 predicts rotation rates of $n_2 = 15,957$ RPM for the low-density test conditions of $\rho_2 = 0.012$ kg/m^3. This is close to no-load conditions, which can be explained by the drastically lower densities and reduced torque demand on the motor. This means that this fan model is expected to run $\sim 18\%$ faster in Martian-density environments compared to nominal ambient conditions, which was confirmed by the sub-scale test campaign. This increase in rotation rate was accounted for when determining the *Re* number for the test conditions for the fan model used in this work.

Heat transfer considerations

Heat transfer properties of a fluid are also a function of the fluid density, which can be critical for air cooling applications as decreasing gas density directly affects mass flow as well as the heat transfer coefficient. While these types of fans are typically used for cooling separate electronic components, the heat transfer characteristics are here closer analyzed to assess the fans' capability to self-regulate the internal heat and maintain acceptable temperature limits when operating in low-density environments.

For forced-air-cooled systems, the rate of convective heat transfer from a surface to the local ambient fluid is described by (Belady 1996):

$$\dot{q}_{conv.} = hA(T_s - T_f) \tag{17}$$

where h is the thermal convection coefficient, A is the area of heat transfer, and T_s and T_f is the temperature of the surface and fluid, respectively. To avoid confusion with the flow rate, Q, the heat transfer is here denoted as lowercase q. The heat transfer coefficient, h, can further be expressed in dimensionless form with the Nusselt number (Nu):

$$Nu = \frac{hD}{k} \tag{18}$$

where k is the conductivity of the fluid and D the system geometry, both of which are assumed independent of density. Thus, the heat transfer coefficient is proportional to the Nusselt number, which is highly dependent on the flow structure and generally a function of Reynolds number and Prandtl number $Nu = Nu(Re, Pr)$ for forced convection. For laminar and fully developed turbulent flow in a circular duct the Nusselt number based on empirical correlations is given by:

$$Nu = 4.36 = const. \quad Re < 2000 \text{ (laminar)} \tag{19}$$

$$Nu = 0.023 Re^{0.8} Pr^{0.4} \quad Re > 10000 \text{ (turbulent)} \tag{20}$$

where Pr is the Prandtl number (0.7 for air) and $Nu_{lam} \ll Nu_{turb}$. Expressed in terms of the fluid density and flow rate, the heat transfer in a turbulent flow is:

$$h = \text{const.}\ \rho^{0.8} Q^{0.8} \quad Re > 10000 \text{ (turbulent)} \tag{21}$$

Consequently, a decreasing fluid density reduces the heat transfer coefficient and thus forced convection if the flow can be considered turbulent. More substantial changes in density can, furthermore, lead the flow to being laminar, where the heat transfer coefficient is no longer varying with density, however, is considerably lower than in turbulent flows.

Equally, the heat capacity of a fluid, q_{hc}, scales with the fluid density, which can be rewritten in terms of the volumetric flow rate:

$$\dot{q}_{hc} = \dot{m} C_p (T_{f,o} - T_{f,i}) = \rho Q C_p (T_{f,o} - T_{f,i}) \tag{22}$$

where C_p is the specific heat of the surrounding fluid and $(T_{f,o} - T_{f,i})$ the temperature difference between inlet and outlet. Hence, at constant volume flow, the advection of heat decreases drastically with density due to a reduced mass flow, resulting in an increased temperature rise from inlet to outlet of the system, ΔT, for dissipating the same amount of heat, which in turn can negatively affect the convective cooling.

From the above-presented analysis, it can be concluded that the fluid density has severe adverse effects on the advection of heat by the forced air as well as the efficiency of heat exchange from the components to the fluid itself. Meanwhile, it was established that the fan power consumption similarly decreases with fluid density, leading to reduced currents and, therefore, reduced resistive heating of the fan unit. However, the maximum fan power consumption cannot be assumed to decrease proportional to the density as suggested by the fan laws ($\rho_2/\rho_1 < P_2/P_1$), since fan efficiency decreases with Reynolds number and fans run faster due to reduced loading. Assuming that the heat generated by the fan unit is proportional to the power consumption (i.e., neglecting frictional heating and assuming a constant electric efficiency) and assuming a constant heat capacity C_p, an estimate for the magnitude of the component and fluid temperature at 100% duty cycle for ambient and Martian test conditions can be made. Using Eqs. 17, 21, and 22 and performance values from Table 3, the temperature deltas are:

$$\begin{aligned} \frac{(T_s - T_f)_2}{(T_s - T_f)_1} &= \frac{\dot{q}_{conv,2}}{\dot{q}_{conv,1}} \frac{h_1}{h_2} \\ &= \frac{\lambda_2}{\lambda_1} \frac{\rho_2}{\rho_1} \left(\frac{n_2}{n_1}\right)^3 \left(\frac{\rho_1}{\rho_2}\right)^{0.8} \left(\frac{\phi_1}{\phi_2} \frac{n_1}{n_2}\right)^{0.8} \approx 2.3 > 1 \end{aligned} \tag{23a}$$

$$\begin{aligned} \frac{(T_{f,o} - T_{f,i})_2}{(T_{f,o} - T_{f,i})_1} &= \frac{\dot{q}_{hc,2}}{\dot{q}_{hc,1}} \frac{\dot{m}_1}{\dot{m}_2} \\ &= \frac{\lambda_2}{\lambda_1} \frac{\rho_2}{\rho_1} \left(\frac{n_2}{n_1}\right)^3 \left(\frac{\rho_1}{\rho_2}\right) \left(\frac{\phi_1}{\phi_2} \frac{n_1}{n_2}\right) \approx 5.9 > 1 \end{aligned} \tag{23b}$$

As a consequence of this, when fans are operating in an environmental chamber at room temperature and low density, they are expected to experience slower initial temperature rise due to reduced power consumption compared to ambient conditions, whereas the reduced convective cooling and heat capacity will lead to higher steady-state component and exhaust temperatures, both of which are undesirable, because it can affect long-term component reliability and changes the freestream temperature. It should be noted that for the convective cooling in Eq. 23a the flow was assumed fully turbulent for both scenarios, which may not necessarily be true. If the flow is indeed laminar under low-density

conditions, the temperature difference is likely to be even higher. It also needs to be mentioned here that the above presented analysis is greatly simplified, but the general trends outlined here are supported by experimental findings of this study.

Ambient rotorcraft forward flight test

Rotorcraft operation introduces significant induced velocity perpendicular to the main freestream flow direction and is thus particularly sensitive to the overall test section size, adding further constraints on the required test section size. Here, experiments using a rotor model with similar size as the Ingenuity system were performed to further examine the minimum size requirements for a multi-fan wind tunnel.

Figure 11 depicts the experimental setup, in which, a single-rotor model ($D = 1.14$ m) with collective and cyclic pitch control was installed in front of the Caltech multi-fan wind tunnel. The rotor was oriented upside down with the rotor wake directed upward to circumvent the problem of ground effect aerodynamics. Orientation and size of the rotor model were chosen similar to the anticipated fixed-mounted forward flight tests of Ingenuity. The rotor plane was oriented parallel to the floor for simplicity and only collective pitch control was utilized. The rotor mounting was additionally instrumented with load cells for lift and drag recordings.

Using the wind tunnel's unique capability of addressing and controlling each fan individually allowed us to actively reduce the overall test section horizontal and vertical dimensions by switching off columns or rows fans, respectively. Other relevant operational parameters (freestream velocity, rotor rotation rate and rotor collective pitch) remained constant throughout each test run, which permitted a direct assessment of the critical wind tunnel size at which edge effects become significant. These direction of size reductions occurred from below the rotor plane (intake of the rotor), from the sides, or from above the rotor plane (wake) separately in different test runs. For each test, the rotor was spooled up to a constant value of 2700 RPM, similar to the Ingenuity system, and the collective pitch was adjusted for a maximum allowable rotor thrust of approximately 97 N. Once the rotor reached steady-state operational conditions after an initial settling phase, all 36x36 fan units of wind tunnel were set to a predetermined, uniform velocity in the range of 5-12 m/s and the full-tunnel-lift and -drag baselines for the given velocity were quantified. Subsequently, maintaining a constant freestream velocity, rotor rotation rate and collective pitch, the operational fan wall size was incrementally reduced by switching off individual rows or alternatively columns of fans. After each wind tunnel size modification, the mean rotor forces and standard deviation were measured over 15 second periods. This process is schematically depicted in Fig. 11 (right). The experimental procedure was repeated for multiple freestream velocities for each of the three reduction directions (intake, sides, wake). Figure 12 shows the rotor forces against the horizontal or vertical distance from the rotor center to the wind tunnel edge of interest. In an attempt to generalize data, a scaling

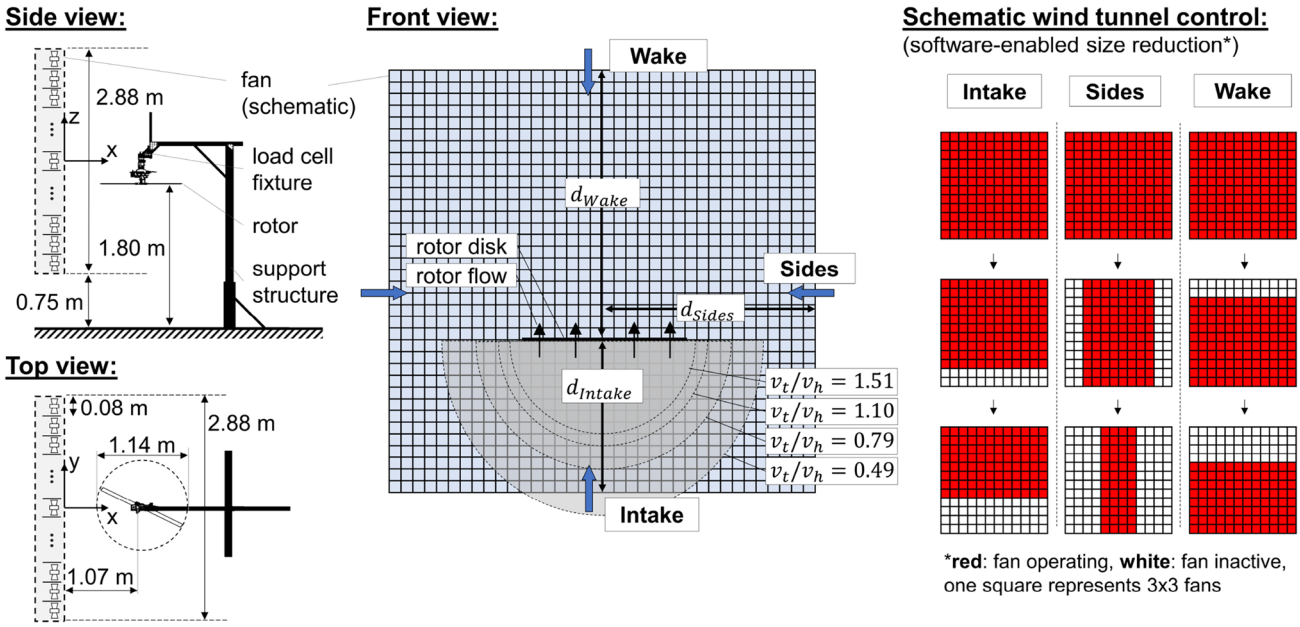

Fig. 11 Setup and terminology for rotorcraft wind tunnel sizing experiments including illustration of theoretical intake areas for different velocity ratios, and schematic visualization of the wind tunnel size reduction process. Note the rotor is oriented upside down

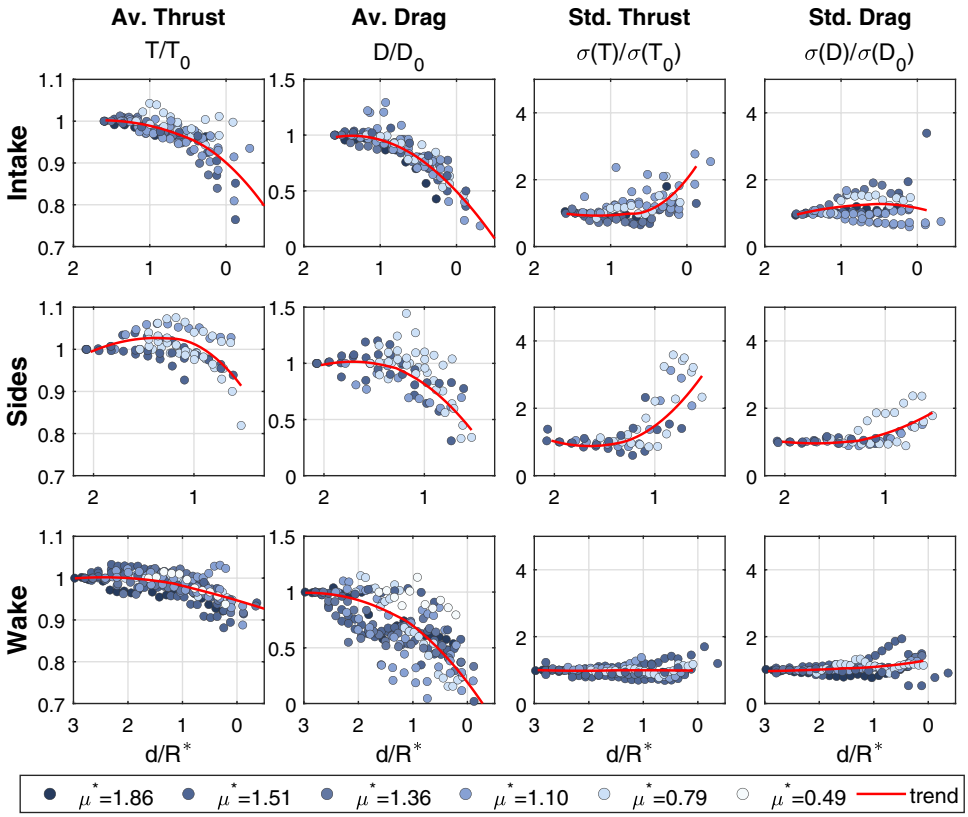

Fig. 12 Rotor force measurements vs. wind tunnel size (distance between rotor axis and wind tunnel edge) for different directions, refer to Fig. 11 for terminology

distance based on fluid mass flow through the rotor and tunnel was derived. With the mass flow through the rotor and the induced velocity of the rotor in hover according to the momentum theory approach being (Johnson 2012):

$$V_h = \sqrt{\frac{T}{2\,\rho\,A_r}} \tag{24}$$

where T is the rotor thrust, and A_r the rotor disk area, i.e., the area swept out by the blades. It follows that the mass flow through the rotor is:

$$\dot{m} = \rho\,A_r\,V_h = \sqrt{\frac{T\,\rho\,A_r}{2}} \tag{25}$$

When assuming that the wind tunnel has to supply, at absolute minimum, the same mass flow of horizontally accelerated flow, the corresponding tunnel area becomes:

$$\dot{m} = \rho\,V_t\,A_t = \rho\,V_h\,A_r \tag{26}$$

$$A_t = \frac{V_h}{V_t}A_r = \sqrt{\frac{T\,A_r}{2\,\rho\,V_t^2}} \tag{27}$$

where A_t is the minimum planform wind tunnel area and $V_t = V_\infty$ the wind tunnel freestream velocity. Since the area ratio is directly related to the velocity ratio of the freestream to the induced velocity of the rotor, the following normalization of the forward speed (tunnel velocity) is defined, which is similar to the advance ratio $\mu = V_\infty/\Omega R$.

$$\mu^* = \frac{V_t}{V_h} \tag{28}$$

For the geometry of A_t, a further assumption is made that all flow is ingested from the intake direction of the rotor plane, which is below the rotor plane in this case, since the rotor is mounted upside down. The geometry minimizing the overall distance to the center of the rotor is a half circle with the radius:

$$R^* = \sqrt{\frac{2A_t}{\pi}} = \sqrt{\frac{2A_r}{\pi} * \frac{V_h}{V_t}} = \sqrt{\frac{1}{\pi}\sqrt{\frac{2T\,A_r}{\rho\,V_t^2}}} \tag{29}$$

Figure 11 (middle) illustrates the derived projected intake areas for the given experimental conditions, a thrust of $T = 97$ N and various, representative velocity ratios V_t/V_h. It can be seen that an increase in wind tunnel freestream velocity results in a decrease in required wind tunnel size. The hypothesis was qualitatively confirmed through the use of

smoke visualization, in which glycerol smoke was injected at various points and freestream velocities upstream of the wind tunnel. It could be observed that only smoke injected within the confines of the projected intake radius R^* entered the rotor disk. It is worth mentioning that the expression in Eq. 29 is merely a first-order approximation and does not necessarily reflect true flow characteristics. For instance, even fluid not passing directly through the rotor disk can influence the rotor aerodynamics.

Nonetheless, the expression from Eq. 29 was used as a scaling quantity to normalize the distance between the rotor center and the wind tunnel edge in Fig. 12, which shows the measured rotor thrust and drag with varying wind tunnel size. The abscissa denotes the vertical/horizontal distance from the rotor center to the edge of the wind tunnel normalized by the expression of R^* (see Fig. 11 for terminology). It is worth mentioning again that only the distance of interest was reduced, while the other two distances remained unchanged at the full-wind-tunnel-dimension. The ordinate denotes the average thrust and drag measurements as well as the standard deviation relative to the full-tunnel baseline values for various μ^*.

The normalized experimental data shows only marginal changes in the rotor forces when wind tunnel size is varied above the critical distance of $d/R^* = 1$ on the intake and sides. When the distance from the rotor center to the wind tunnel edge is reduced below this critical value, significant effects on the aerodynamic forces can be observed. This is particularly evident in the thrust and drag measurements. Furthermore, wind tunnel size reductions below R^* lead to pronounced force fluctuations, as seen in the standard deviation of forces. Both, the reduction in thrust and strong fluctuations, are believed to derive from the blade tips entering the wind tunnel edge shear layer during the rotation. It should be noted here that effects of insufficient wind tunnel size can already be observed for values slightly greater than $d/R^* = 1$ and according margins should be factored in. This is consistent with the results shown in Fig. 8, where edge effects and high levels of flow turbulence were found to occur for spanwise distances of $y > 0.4L$. Meanwhile, even though it was previously assumed that flow is only ingested through the rotor from the intake side of the rotor plane, the data indicates that the wind tunnel dimension on the wake side of the rotor plane is quite relevant as well. However, identification of the critical wind tunnels dimension on the wake side of the rotor yields more ambiguous results. In this case, thrust measurements start to diverge from full-tunnel values at $d \approx 1R^*$, but drag measurements at $d \approx 2R^*$. Given the considerably lower drag forces compared to the thrust, causing the drag to be more prone to measurement noise, it is unclear whether the critical value for the wake side should be based on the thrust or drag measurements. Regardless, a conservative minimum dimension in the wake direction is $d = 2R^*$. When observing the standard deviation of both forces, it can be noted that reducing the wind tunnel dimension from the wake direction introduces only minor force fluctuations, starting at $d/R^* = 1$.

The insights obtained by these ambient reference measurements help to establish absolute minimum requirements for the size of a multi-fan wind tunnel. Analysis of the unobstructed flow field in the main paper outlined a functional test section within the bounds of $y, z = [-0.4L, 0.4L]$ in the spanwise and vertical direction, and $6.75D < x < 1.4L$ in the streamwise direction. When flow uniformity and low turbulence intensity are of concern for the application, downstream distances of $x > 20D$ to the face of the fan wall should be maintained. Rotorcraft operation creates further constraints on the minimum wind tunnel size, those being that the freestream flow has to supply a sufficient mass flow to feed the rotor. The minimum wind tunnel edge distances from the rotor center outlined here are $d/R^* > 1$ on the intake side of the rotor plane and within the rotor plane (sides) as well as $d/R^* > 2$ on the wake side. Assuming a horizontal or inverted orientation of the rotorcraft, this yields an overall wind tunnel size of $2R^* \times 3R^*$ (W x H). Insufficient wind tunnel sizing may introduce significant edge effects causing erroneous force readings and strong fluctuations.

In accordance with these dimensioning guidelines, the recommended minimum wind tunnel size for the Ingenuity Mars Helicopter forward flight tests could be established for the given geometric and operational parameters provided in Sect. 3.1 ($m = 1.8$ kg, $D = 1.21$ m, height=0.8 m, g = 3.72 m/s^2), as well as an atmospheric full-scale test density of $\rho = 0.019$ kg/m^3, and a freestream velocity of 10 m/s. For the static rotorcraft model to be geometrically placed within the functional test section, a wind tunnel size of 1.5 m x 1.0 m (W x H) is required. Equation 29 yields a projected intake radius for the Ingenuity system of $R^* = 0.95$ m, requiring a wind tunnel size of 1.9 m x 2.85 m (W x H), which exceeds the static minimum requirements. Due to pragmatic reasons, including a limited number of sourecable fans within a short time period and the time intensive modifications for contamination requirements, the full-scale facility dimensions were limited to 1.68 m x 1.68 m. As these dimensions fall short of the critical size outlined in Fig. 12, wind tunnel edge effects were expected to occur. Consequently, all experimental data obtained in the Ingenuity forward flight tests was sufficiently margined.

Acknowledgements Reference herein to any specific commercial product, process, or service by trade name, trademark, manufacturer, or otherwise, does not constitute or imply its endorsement by the United States Government or the Jet Propulsion Laboratory, California Institute of Technology. The authors would like to thank the JPL Ingenuity Team for the implementation of the low-density wind tunnel in the 25-ft chamber. The authors additionally wish to thank various people

for their contribution to this project: Alejandro Stefan Zavala, for developing the operating software for the wind tunnel systems; Peter Renn, for assisting during the ambient flow measurements; Manuel Gallegos, for the sub-scale system chamber integration and testing; and Dave Natzic, for his assistance during the sub-scale chamber tests. The authors would also like to thank associate editor Jerry Westerweel, and reviewers Ralph Lorenz and an anonymous reviewer for their constructive feedback that substantially improved the quality of this manuscript.

Author contributions Conceptualization: Jason Rabinovitch; Methodology: Marcel Veismann, Christopher Dougherty, Jason Rabinovitch; Formal analysis and investigation: Marcel Veismann, Christopher Dougherty, Jason Rabinovitch; Writing—original draft preparation: Marcel Veismann; Writing—review and editing: Marcel Veismann, Christopher Dougherty, Jason Rabinovitch; Funding acquisition: Jason Rabinovitch; Resources: Jason Rabinovitch; Supervision: Morteza Gharib, Amelia Quon.

Funding Parts of this research were carried out at the Jet Propulsion Laboratory, California Institute of Technology, under a contract with the National Aeronautics and Space Administration (80NM0018D0004).

Availability of data and material Due to governmental sponsorship, the availability of data and material for external use will be evaluated on a case-by-case basis.

Declarations

Conflict of interest The authors declare that they have no conflict of interest.

Code availability Not applicable.

References

AMCA Air Movement and Control Association International (2016) Certified ratings program product rating manual for fan air performance. AMCA Publication pp 211–213 (Rev. 09–17)

Ament G, Koning WJF (2018) Isolated rotor forward flight testing from one atmosphere down to Martian atmospheric densities

Anyoji M, Nagai H, Asai K (2009) Development of low density wind tunnel to simulate atmospheric flight on mars. In: 47th AIAA Aerospace Sciences Meeting including The New Horizons Forum and Aerospace Exposition, p 1517. https://doi.org/10.2514/6.2009-1517

Balaram B, Canham T, Duncan C, Grip HF, Johnson W, Maki J, Quon A, Stern R, Zhu D (2018) Mars helicopter technology demonstrator. In: 2018 AIAA Atmospheric Flight Mechanics Conference, https://doi.org/10.2514/6.2018-0023

Bardera R, Sor S, García-Magariño A (2020) Aerodynamics of mars 2020 rover wind sensors. In: Mars Exploration, IntechOpen, https://doi.org/10.5772/intechopen.90912

Belady CL (1996) Design considerations for air cooling electronic systems in high altitude conditions. IEEE Trans Compon Packaging Manuf Technol 19(4):495–500. https://doi.org/10.1109/STHERM.1996.545100

Boetcher S, Sparrow EM (2007) Limitations of the standard bernoulli equation method for evaluating pitot/impact tube data. Int J Heat Mass Transfer 50(3–4):782–788. https://doi.org/10.1016/j.ijheatmasstransfer.2006.01.044

Bogdanović-Jovanović JB, Milenković DR, Spasić ŽT, Svrkota DM (2016) Performance of low-pressure fans operating with hot air. Thermal Sci 20(suppl. 5):1435–1447. https://doi.org/10.2298/TSCI16S5435B

Casey M (1985) The effects of reynolds number on the efficiency of centrifugal compressor stages. J Eng Gas Turbines Power 107(2):541–548. https://doi.org/10.1115/1.3239767

Delta Electronics, Inc (2015) Specification for approval. GFM-0812DUB7S datasheet

Delta Electronics, Inc (2016) Specification for approval. GFC0812DW-TD2G datasheet

Grip HF, Scharf DP, Malpica C, Johnson W, Mandic M, Singh G, Young LA (2018) Guidance and control for a mars helicopter. In: 2018 AIAA Guidance, Navigation, and Control Conference, p 1849. https://doi.org/10.2514/6.2018-1849

Harrell J, Largould M (1969) The 25-ft space simulator at the jet propulsion laboratory. Technical Report 32-1415

Heß M, Pelz PF (2010) On reliable performance prediction of axial turbomachines. Turbo Expo Power Land Sea Air 44021:139–149. https://doi.org/10.1115/GT2010-22290

Jin X, Ma EW, Chow TW, Pecht M (2012) An investigation into fan reliability. In: Proceedings of the IEEE 2012 Prognosticsand System Health Management Conference (PHM-2012 Beijing), IEEE, pp 1–7

Johnson W (2012) Helicopter theory. Courier Corporation

Leovy C (2001) Weather and climate on mars. Nature 412(6843):245–249. https://doi.org/10.1038/35084192

McCoy M, Wadcock AJ, Young LA (2016) Documentation of the recirculation in a closed-chamber rotor hover test. Ames Research Center, Moffett Field CA 94035, USA, NASA/TM–2016-219162

NASA (2014) Nasa's mars exploration program. https://mars.nasa.gov/. Accessed September 12, 2020

Noca F, Catry G, Bosson N, Bardazzi L, Marquez S, Gros A (2019) Wind and weather facility for testing free-flying drones. In: AIAA Aviation 2019 Forum, p 2861. https://doi.org/10.2514/6.2019-2861

Ozono S, Ikeda H (2018) Realization of both high-intensity and large-scale turbulence using a multi-fan wind tunnel. Exp Fluids 59(12):187. https://doi.org/10.1007/s00348-018-2647-4

Pelz P, Stonjek S (2014) Introduction of an universal scale-up method for the efficiency. ASME Turbo Expo. https://doi.org/10.1115/GT2014-25403

Petrosyan A, Galperin B, Larsen SE, Lewis S, Määttänen A, Read P, Renno N, Rogberg L, Savijärvi H, Siili T et al (2011) The martian atmospheric boundary layer. Rev Geophys. https://doi.org/10.1029/2010RG000351

Rütschi K (1958) Zur wirkungsgradaufwertung von strömungsmaschinen, verhalten einer einzelmaschine und einer reihe von maschinen verschiedener grösse. Schweiz Bauztg 76:603–606. https://doi.org/10.5169/seals-64061

Simon H, Bülskämper A (1984) On the evaluation of reynolds number and relative surface roughness effects on centrifugal compressor performance based on systematic experimental investigations. J Eng Gas Turbines Power 106(2):489–498. https://doi.org/10.1115/1.3239592

Strub R, Bonciani L, Borer C, Casey M, Cole S, Cook B, Kotzur J, Simon H, Strite M (1987) Influence of the reynolds number on the performance of centrifugal compressors. J Turbomach 109(4):541–544. https://doi.org/10.1115/1.3262145

White B (1987) A low-density boundary-layer wind tunnel facility. In: 25th AIAA Aerospace Sciences Meeting, p 291. https://doi.org/10.2514/6.1987-291

Wilson C, Camilletti A, Calcutt S, Ligrani P (2008) A wind tunnel for the calibration of mars wind sensors. Planetary Space Sci 56(11):1532–1541. https://doi.org/10.1016/j.pss.2008.05.011

Wright T (1999) Fluid machinery: performance, analysis, and design. CRC Press, Cambridge

Zhang L, Liu G, Leng W (2018) Development of the simulation & experiment system for martian atmosphere simulation environment box. In: MMSA 2018, Atlantis Press, https://doi.org/10.2991/mmsa-18.2018.14